THE AMERICAN SOCIETY OF MECHANICAL ENGINEERS
Three Park Avenue, New York, N.Y. 10016-5990

99-GT-97

Propagation of Multiple Short Length-Scale Stall Cells in an Axial Compressor Rotor

M. Inoue, M. Kuroumaru, T. Tanino, and M. Furukawa
Department of Energy and Mechanical Engineering,
Kyushu University,
Fukuoka,Japan

Abstract

Evolution and structure of multiple stall cells with short length-scale in an axial compressor rotor have been investigated experimentally. In a low-speed research compressor rotor tested, a short length-scale stall cell appeared at first, but did not grow rapidly in size unlike a so-called "spike-type stall inception" observed in many multi-stage compressors. Alternatively, the number of cells increased to a certain stable state (a mild stall state) under a fixed throttle condition. In the mild stall state the multiple stall cells, size of which was on the same order of the inception cell (a few blade spacings), were rotating at 72 % of rotor speed and at intervals of 4.8 blade spacings. With further throttling, a long length-scale wave appeared overlapping the multiple short length-scale waves, then developed to a deep stall state with a big cell.

In order to capture the short length-scale cells in the mild stall state, a so-called 'double phase-locked averaging technique' has been developed, by which the flow field can be measured phase locked to both of the rotor and the stall cell rotation. Then, time-dependent ensemble averages of the 3D velocity components upstream and downstream of the rotor have been obtained with a slanted hot-wire, and the pressure distributions on the casing wall with high response pressure transducers.

By a physically plausible explanation for the experimental results, a model for the flow mechanism of the short length-scale stall cell has been presented. The distinctive feature of the stall cell structure is on the separation vortex bubble with a leg traveling ahead of the rotor, with changing the blade in turn on which the vortex leg stands.

Introduction

It is said there are two types of stall inception in axial compressors. The first one is characterized by long length-scale disturbances (Garnier et al., 1991) for which two-dimensional linearized stability analyses are available (Moore and Greitzer, 1986, Weigl et al., 1997). The second one is characterized by a short length-scale disturbance known as "spike" (McDougall et al., 1990). Sometimes, the coupling of these inception types occurs (Day, 1993). Recently, Day, et al. (1997) investigated the stall inception for several European aero-engine type compressors, and found a new type of high frequency stall inception in two compressors operating at full speed. Inferred from the experimental results of low speed compressor testing at the Whittle Laboratory, in which multiple part-span stall cells rotated at 82 % of rotor speed and at intervals of 5 blade spacings, they thought that the high frequency waves were resulted from multiple part-span stall cells. The multiple wave disturbances due to part-span stall cells were also reported in the low speed compressor test rig by Mathioudakis and Breugelmans (1985). Silkowski (1995) observed them in the low-speed 4-stage compressor test rig with a mismatched stage condition, and mentioned that the short length-scale disturbances (spike) appeared and disappeared sporadically near the stall condition at first, then the number of the spikes increased with the flow rate decreasing, and finally multiple spikes appeared at intervals of 4.5 blade spacings rotating at roughly 70 % of rotor speed at a lower flow rate.

In a low-speed compressor test rig of Kyushu University, a similar phenomenon has occurred in evolution of rotating stall. In this paper, formation process of the multiple part-span cells with short

Nomenclature

C_p : pressure coefficient
LPF : low-pass filtered
p' : deviation of pressure from ensemble average
p_a : stagnation pressure in inlet chamber
p_c : casing wall pressure
r : radius
r_t : radius of blade tip
T_p : stall cell location relative to a blade spacing
u_t : blade tip speed
Δ : an increment of gray scale in the figures
ρ : density
ϕ : flow rate coefficient (the mean axial velocity divided by u_t)
ψ : pressure coefficient (the total pressure rise divided by $pu_t^2/2$)

Presented at the International Gas Turbine & Aeroengine Congress & Exhibition
Indianapolis, Indiana — June 7–June 10, 1999
This paper has been accepted for publication in the Transactions of the ASME
Discussion of it will be accepted at ASME Headquarters until September 30, 1999

length-scale and its coalescing process into a big rotating stall cell are presented firstly, based on the measurement data by pressure transducers mounted on the casing wall near the rotor leading edge. Secondly, a so-called 'double phase-locked averaging' (DPLA) technique is proposed to capture the short length-scale stall cell by a slanted hot-wire and high response pressure transducers, with which 3D flow fields before and behind the rotor and the casing wall pressure distribution can be obtained synchronously with both of the rotor and the cell rotation. Lastly, a flow mechanism of the short length-scale stall cell is discussed based on the time-dependent ensemble averages of the three-dimensional velocity components upstream and downstream of the rotor and the casing wall pressure distributions.

Experimental Facility and Instrumentation

A schematic view of the test section of the low-speed research compressor is shown in Fig. 1. It consists of a 449-mm-dia rotor with hub/tip ratio of 0.7, two cantilevered stators upstream and downstream of the rotor, and inlet and outlet guide vanes. The rotor comprises 24 blades designed for a constant whirl angle of absolute inlet flow and 50 % reaction at mid span. The two stators consisting of 22 blades are geometrically identical, and the inlet guide vanes are designed for the same exit flow angle distribution as the rotor in order to simulate a middle stage of a compressor. The gap between the rotor and the stator is about a half of the blade height which is considerably larger than the actual compressor stages to make a survey of the flow field. The compressor stage has the flow rate coefficient of $\phi = 0.5$, and the pressure coefficient of $\psi = 0.4335$ at the design point. The blade profile used is of NACA 65 series for the rotor, two stators and outlet guide vanes,

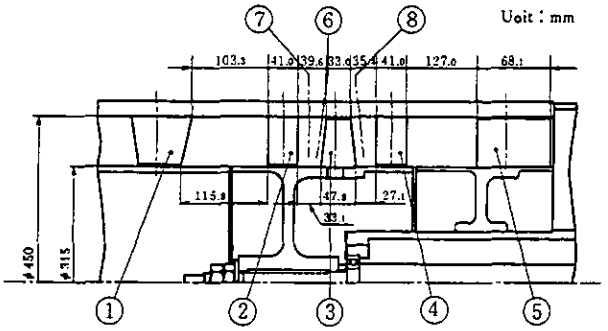

1	I.G.V.	5	O.G.V.
2	Stator1	6	Measurement Locaion S1
3	Rotor	7	Measurement Location S2
4	Stator2	8	Measurement Location S3

Fig. 1 A schematic view of test section.

Table 1 Design specifications of rotor and stator

Rotor	r/r_t	β_1	β_2	σ	C_{l0}	γ	τ
Tip	1.000	57.2	45.6	0.850	0.909	48.9	6.0
	0.925	53.3	38.2	0.919	1.045	43.2	8.0
Mid	0.850	48.8	29.0	1.000	1.215	36.2	10.0
	0.775	43.5	18.0	1.097	1.415	27.7	12.0
Hub	0.700	37.4	5.5	1.214	1.618	17.9	14.0

Stator	r/r_t	α_1	α_2	σ	C_{l0}	γ	τ
Tip	1.000	48.3	29.0	0.779	1.360	35.7	10.0
	0.925	48.4	29.0	0.842	1.331	35.9	10.0
Mid	0.850	48.7	29.0	0.917	1.307	36.2	10.0
	0.775	49.2	29.0	1.005	1.289	36.4	10.0
Hub	0.700	49.8	29.0	1.113	1.278	36.5	10.0

* isolated airfoil lift coefficient of NACA65 profile camber line at zero angle of attack in potential flow

α_1 : inlet flow angle
α_2 : exit flow angle
β_1 : inlet flow angle
β_2 : exit flow angle
σ : solidity
C_{l0} : lift coefficient *
γ : stagger
τ : maximum thickness (%)

and of NACA 63 series for the inlet guide vanes. The blade tip clearance is 0.5 mm (0.75 percent of blade height) for the rotor and stators. Additional information for the bladings is shown in Table 1.

The stage performance was evaluated for a combination of the rotor and the downstream stator. The total pressure rise of the stage was obtained from the pressure difference between the inlet and outlet chamber by subtracting the aerodynamic losses of other elements which had been obtained in a preliminary experiment without the rotor and the downstream stator. The flow rate was measured by a flow nozzle connecting with outlet chamber (See Inoue, et al, 1993).

A single slanted hot-wire and a 5-hole pressure probe are used to survey internal flows in the radial direction upstream and downstream of the rotor, and both in the radial and circumferential direction downstream of the stators.

For measuring the casing wall pressure distribution, 14 high response pressure transducers (Kulite XCS-062) are mounted on the casing wall to cover the measuring points from 24.6 mm upstream of the rotor leading edge to 20.4 mm downstream of the rotor trailing edge in the axial direction. One of the pressure transducers near the rotor leading edge is used to detect rotating stall inception of the rotor and to observe a transient phenomenon of the stall cell development. A trigger pulse of the stall inception is taken by setting a threshold level for the low-pass filtered (LPF) signal of the pressure sensor for which the blade passing frequency has been removed. Another pressure sensor is located at 90° apart in the circumferential direction to measure the number of stall cells and their rotating speed.

Evolution of Multiple Short Length-Scale Stall Cells

Pressure-rise characteristics of the compressor stage Figure 2 shows the pressure-rise characteristics of the compressor stage tested. The pressure coefficient ψ is the maximum at the flow rate coefficient of $\phi = 0.380$. With throttling from $\phi = 0.380$ to 0.346 the pressure coefficient reduces, but in this flow range any signal indicating stall inception is not observed in the LPF output of the pressure sensor on the casing wall near the rotor leading edge. The cause of the pressure reduction was examined by flow surveys downstream of the rotor and the stator using the 5-hole pressure probe. The averaged total pressure at the rotor exit increases from $\phi = 0.400$ to 0.355 (the figure omitted). But, as shown in Fig. 3 which shows the total pressure distributions at the downstream stator exit for $\phi = 0.400$ and 0.355, a corner stall grows noticeably between a cantilevered stator blade and the casing wall at $\phi = 0.355$. The pressure reduction is

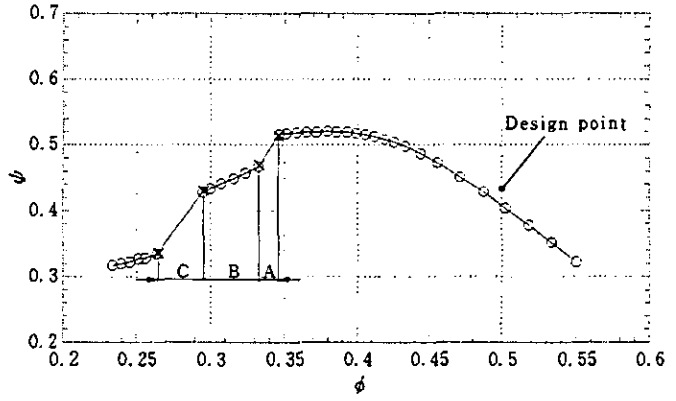

Fig. 2 Stage performance of compressor stage tested.

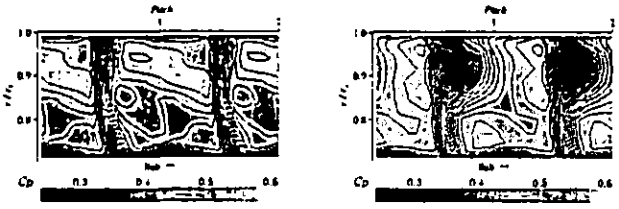

(a) $\phi = 0.400$ (b) $\phi = 0.355$

Fig.3 Total pressure distoribution downstream of stator.

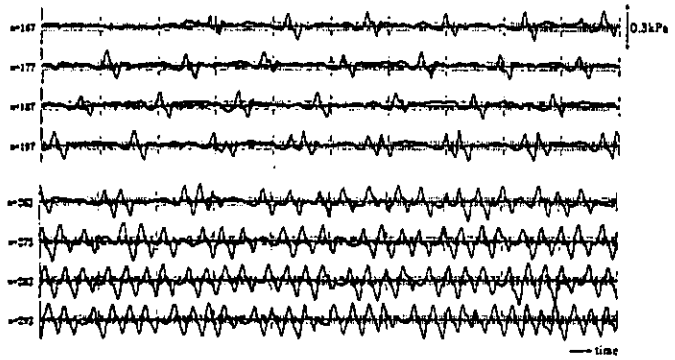

Fig. 4 Low-pass filtered pressure trace near rotor leading edge in flow range A.

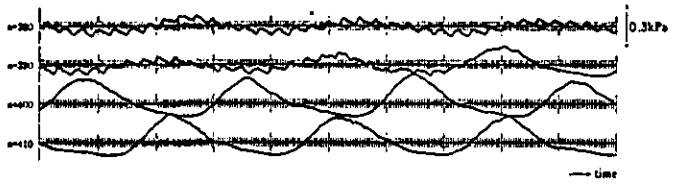

Fig. 5 Low-pass filtered pressure trace near rotor leading edge in flow range C.

mainly caused by growth of this stator corner stall. Stall inception of the rotor is detected at $\phi = 0.346$, from where the flow rate decreases by itself (without throttling) to $\phi = 0.332$ in around a hundred rotations of the rotor, and the pressure drops from $\psi = 0.516$ to 0.470. As the flow rate decreases from $\phi = 0.332$ to 0.295 by closing the throttle carefully, the pressure reduces gradually to $\psi = 0.428$, and then, jumps to $\psi = 0.335$ at $\phi = 0.264$. In this paper, the flow ranges from $\phi = 0.346$ to 0.332, $\phi = 0.332$ to 0.295, and $\phi = 0.295$ to 0.264 are designated as the flow ranges A, B, and C, respectively, for convenience of the following discussion.

Time evolution of casing wall pressure trace Figure 4 shows a time evolution of the casing wall pressure trace with the low-pass filter near the rotor leading edge in the flow range A. The output of LPF pressure is shown against time. For each horizontal line, the short and long vertical lines stand for blade passing and rotor rotations respectively, and n is a number for rotor rotation corresponding to the left vertical line. Immediately the stall inception is detected in the LPF pressure signal, a spiky wave is generated in a rotor rotation with rapid increase followed by rapid decrease in the pressure. Similar wave shapes appear at intervals of 1.36 times of a rotor rotation. Then, the second spiky wave appears next to the first one, and the number of waves increases at unequal intervals with time. Finally, the similar shapes of wave stand in at intervals of about 0.27 times of a rotor rotation. In the flow range B, they keep to be at the same intervals of about 0.27 (the figure is omitted).

A LPF pressure trace in the flow range C is shown in Fig. 5. It is clearly seen that the short length-scale waves and a long length-scale wave are overlapping each other, and turn into a big wave due to a deep stall cell.

Cross-correlation function of two pressure signals In order to examine the number and rotating speed of the stall cells, the LPF pressure signals have been analyzed by a cross-correlation function. Figure 6 (a) shows the LPF pressure traces for two pressure sensors

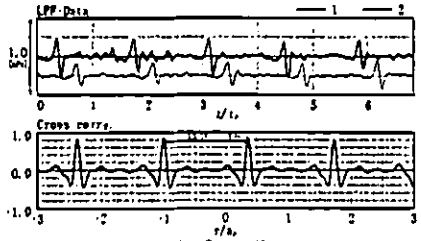

(a) One cell

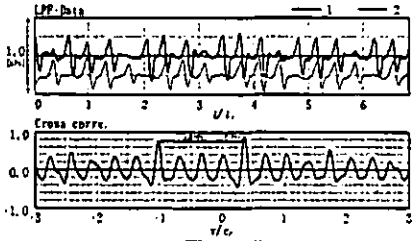

(c) Three cells

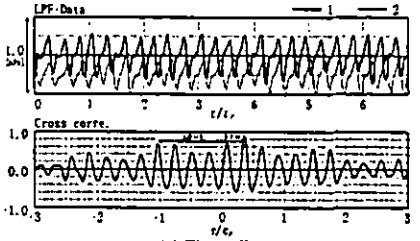

(e) Five cells

Fig. 6 Traces and cross-correlation function of two pressure signals in flow range A.

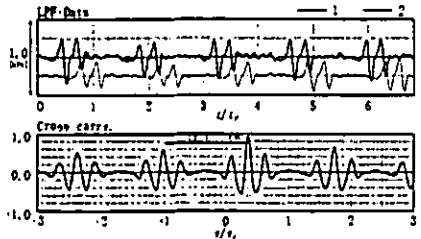

(b) Two cells

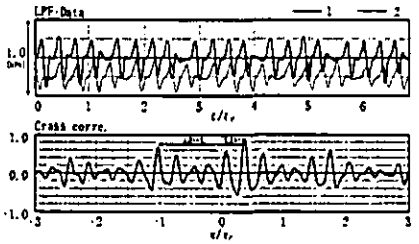

(d) Four cells

t: time τ: time delay t_r, τ_r: rotor period

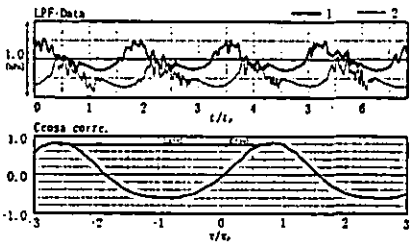

Fig. 7 Traces and cross-correlation function of two pressure signals in flow range C.

located at 90° apart each other in the circumferential direction, and a cross-correlation function of the two signals, when short-length scale waves exist at intervals of 1.36 times of a rotor rotation. From this figure, it is estimated that one cell rotates at 73.4 % of the rotor speed.

If the cells are rotating at nearly constant speed, the number of the cells must be increasing with time until it attains the final condition of the range A. Then, pieces of the pressure trace where the number of cells are expected to be 2, 3, 4 and 5 have been analyzed by the cross-correlation function, respectively. The results are shown in Figs. 6 (b) to (e). From the interval of two large peaks it is found that the rotating speed of the cell decreases a little with the number of cells, and is 72.2 % of the rotor rotation when five cells exist. In the cross-correlation functions of Figs. 6 (b), (c) and (d), the number of small peaks between two large peaks are 2, 3, and 4, respectively. This fact seems to be as if the number of the cells was one more than what had been expected from the LPF pressure traces. This is because the cells stand in at unequal intervals as will be shown by the wavelet analysis described later. One should notice that the number of cells estimated only by the cross-correlation function may be incorrect when they are at unequal intervals.

In the range B, the LPF pressure traces and the cross-correlation function of two pressure signals are similar to Fig. 6 (e) but the corresponding two large peaks are indistinguishable from other peaks in the cross-correlation function (the figure is omitted.). Figure 7 shows the LPF pressure traces and the cross-correlation function in the range C. From this figure, the rotating speed of a big cell is estimated to be 29.3 % of a rotor rotation.

Wavelet analysis The size and the interval of the stall cells are examined by the wavelet transform, which is useful to get local information of disturbances (Farge, 1992).

The wavelet transform of a pressure signal $p(t)$ is defined by

$$W(a,b) = \frac{1}{\sqrt{a}}\int \Psi(T)p(t)dt$$

where, $\Psi(T)$ is a wave let function, a is the scaling parameter, b implies translation and $T(t-b)/a$. When an appropriate function is chosen as $\Psi(T)$, a large value of $W(a, b)$ implies that the disturbance with scale a exists locally around b .

In the present study,

$$\Psi(T) = -\sin(2T)\exp(-T^2)$$

was used since a wave form of this wavelet is similar to the spiky LPF pressure signal observed in Fig. 4.

Figure 8 shows the contour map of $W(a, b)$ in the flow range A. The abscissa is $b/\Delta t$ and the ordinate is a logarithmic scale of $a/\Delta t$ in the opposite direction, where Δt corresponds to 1/120 of a rotor rotation. One cell appears in the first line of the figure, and the second one is generated in the second line. Just after the third cell is generated the intervals are irregular as shown in the third line, but a space appears to every three cells in which the forth cell is generated as shown in the forth line. In several rotations after the fourth cell is generated, a space appears to every four cells to generate the fifth one. The condition of five cells is so stable as to keep it through the flow range B (the figure is omitted). In the ranges A and B, the maximum values of $W(a, b)$ are located at $a/\Delta t \approx 10$. This means that the size of cell is on the order of two blade spacings since the rotor have 24 blades ($a \approx 10\Delta t = 1/12$ of a rotor rotation).

Figure 9 shows the result of the wavelet analysis in the range C. It is clearly seen that a large scale disturbance appears overlapping the five small disturbances in the first line of the figure, and develops with disappearing the small ones. The scale of the large disturbance is on the order of a rotor rotation. This means a single large stall cell is generated in the range C.

Additional discussion Recently, Camp and Day (1998) proposed a simple model to explain the occurrence of long length-scale or spike-type stall inception in a given situation. According to their model, if the peak of the overall pressure characteristic is reached before the critical value of rotor incidence is exceeded anywhere in the compressor then long length-scale oscillations will occur, while, if the critical rotor tip incidence is exceeded before the peak of the overall pressure characteristic is reached then spikes will appear in the overloaded rotor.

In the low-speed compressor stage used in this study, however, the type of stall inception did not conform to their model. A spike appeared at the beginning of the flow range A beyond the peak of the stage characteristic as shown in Fig. 2. Between the peak and the

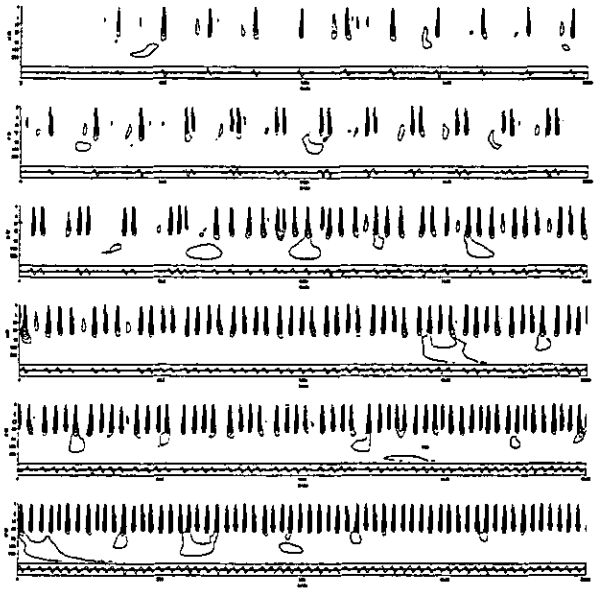

Fig. 8 Result of wavelet analysis in flow range A.

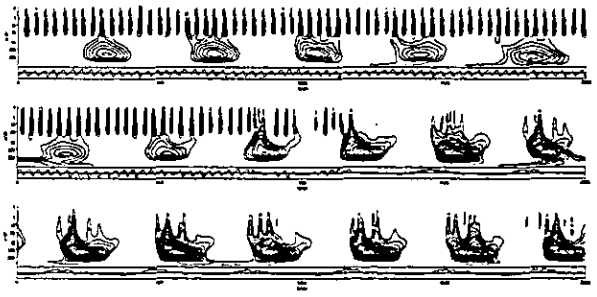

Fig. 9 Result of wavelet analysis in flow range C.

appearance of the spike, any long length-scale wave was not observed. The spike did not grow rapidly in size unlike a so-called "spike-type stall inception". Alternatively, the number of cells increased under a fixed throttle condition, and became five in a certain flow range with keeping the size and the rotating speed.

In the present compressor stage test rig, another rotor and stator, which have swept endbend blades and the same design point, were tested. They were designated as the CEF rotor and the CEF stator (Inoue, et al, 1997). In every combination of the rotor and stator (e.g.: a combination of the CEF rotor and the baseline stator), the situation was similar for the development of rotating stall cells. But, the time in which the number of cells increased from one to five varied depending on the combination of the rotor and stator. When the development of the corner stall in the stator (see Fig. 3(b)) was suppressed by using the CEF stator, the number of cells increased so rapidly that the cross-correlation analysis could not made for each cell number. And it happened very rarely that 6 cells appeared in the flow range B. When the stall inception was delayed by using the CEF rotor and CEF stator, the flow range B was very narrow. The evolution of the rotating stall is very sensitive to the blading geometry. Under a certain condition, a short length-scale cell may grow rapidly in size without increasing the number of cells. Under a different condition, a long length scale wave may appear suddenly without a stable condition of range B. Further investigation will be necessary on this point.

Structure of Short Length-Scale Stall Cell

Double phase-locked averaging technique The size, the pressure wave pattern and the rotating speed of a short length-scale cell near the stall inception are almost the same as those of the multiple stall cells in the flow range B. Therefore, structure of the cells is considered to be identical at the stall inception and in the range B. The structure of short length-scale stall cell at stall inception will be found if the structure of the cells can be captured in the stable condition of the range B.

So far, flow structure of a rotating stall cell was measured by phase-locking data acquisition techniques with the cell rotation (Das and Jiang, 1984; Poensgen and Gallus, 1996; Palomba et al., 1998). These techniques are available for a long length-scale stall cell, since blade geometry has secondary effect for the cell structure. For capturing the short length-scale stall cell, however, it is necessary to acquire the data synchronously with both of the rotor and the cell rotation because the cell size is on the order of a blade spacing length-scale. In this study, the following data sampling and averaging technique is developed to get time dependent ensemble averages.

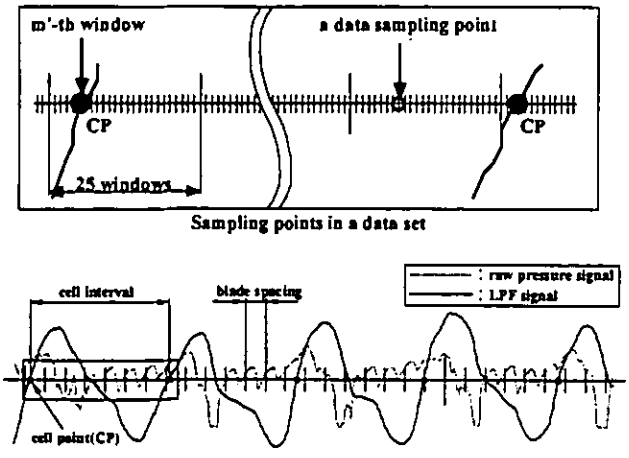

Fig. 10 Illustration of reference location of stall cell.

The data acquisition is made upstream and downstream of the rotor by hot-wire surveys, and on the casing wall by 14 Kulite pressure sensors. At each location, the sensor signals for 600 circumferential sampling points per one rotor rotation are acquired during a sufficient number of the rotor rotations by a sampling system phase-locked to the rotor. Thus, 25 data sampling points are included in a blade spacing since the number of blades is 24 (600/24 = 25).

A location of the stall cell relative to a blade is determined by using these data sampling points and the LPF pressure signal on the casing wall near the rotor leading edge. Namely, a blade spacing is divided into 25 windows by these points as illustrated in the upper part of Fig. 10. The reference point of the cell (cell point) is taken at a point where the LPF pressure signal crosses the zero-line from negative to positive as illustrated in the lower part of Fig. 10. The interval between a cell point and the next cell point corresponds to a period of the cell travelling. A set of data is composed by the data acquired at each sampling point in a cell interval. When the front cell point of the data set is located in the m'-th window ($m' = 1, 2, ..., 25$), the data set is registered in the m'-th data group. All the data belonging to the same data group are averaged at each sampling point. But, one should notice that this averaged data set would not constitute a velocity or a pressure distribution synchronous with the cell rotation, because the rotational speed of the cell is different from the rotor speed. As the data are acquired at a fixed location synchronously with the rotor rotation, the time delay between the cell point and a data sampling point causes a relative location of the stall cell to shift. Therefore, the location of the cell point for each data sampling point should be modified. Such a modification is made by assuming that the cell point would travel at the constant speed. Then, the averaged data at each sampling point for the m'-th data group are rearranged for the m-th data group ($m = 1, 2, ..., 25$) in which the cell point is located in the m-th window at the moment of the data acquisition. The averaged data set in the m-th data group constitutes the time-dependent ensemble averaged distribution at the moment when the cell point crosses in the m-th window. In the present paper, the location of cell relative to a blade is represented by $T_p = (m-1)/25$

The present authors call this sampling and averaging technique the 'double phase-locked averaging (DPLA) technique'. The DPLA technique is applied to flow surveys of velocity vectors upstream and downstream of the rotor by using a single slanted hot-wire. The hot-wire sensor used is a tungsten filament of 5-μm dia., 1 mm effective length and 45-deg slanting angle. The axis of the hot-wire probe is rotated at intervals of 30 deg for 12 orientations of the sensor. At each sensor orientation, the DPLA is made. Since a reverse flow exists in the stall cell, an appropriate set of the 8 ensemble averages of the hot-wire signal is chosen from the 12 averages to evaluate three components of a velocity vector. Namely, three components of the flow velocity are determined from the 8 ensemble averages by solving calibration equations of the hot wire with the least-mean-square method (Kuroumaru, et al., 1982). The DPLA technique is applied also to the casing wall pressure measurement.

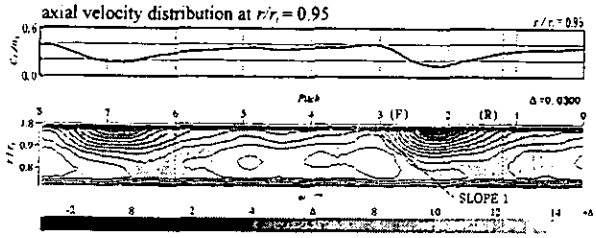

Fig. 11 Axial velocity distributions 25.6mm upstream of the rotor at T_p=0.2.

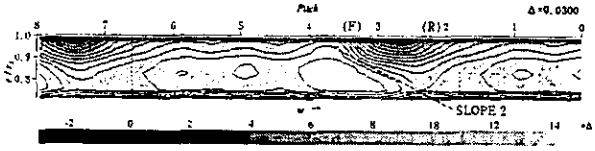

Fig. 12 Axial velocity distributions 25.6mm upstream of the rotor at T_p=0.8.

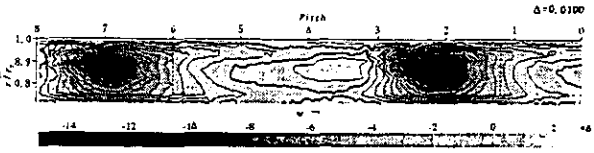

Fig. 13 Radial velocity distribution 25.6mm upstream of the rotor at T_p=0.2.

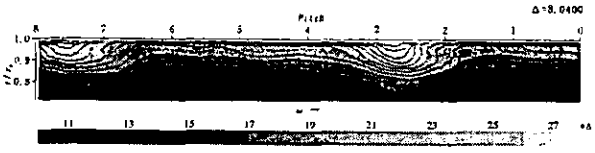

Fig. 14 Tangential velocity distribution 25.6mm upstream of the rotor at T_p=0.2.

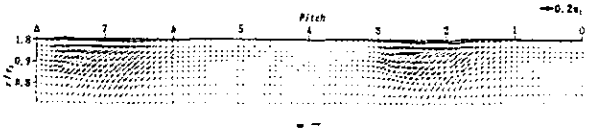

Fig. 15 Secondary flow vector 25.6mm upstream of the rotor at T_p=0.2.

Flow field upstream of the rotor Figures 11 and 12 show the contour maps of the axial velocity component 25.6 mm (77.7 % of the axial blade chord) upstream of the rotor leading edge at T_p = 0.2 and 0.8. The top horizontal line represents the casing wall on which the numbers are marked backward to identify the blade spacings. The bottom line represents the hub wall surface, and the rotor blades rotate from left to right. The axial velocity component normalized by the blade tip speed is indicated by the grey scale. The symbol Δ stands for amount of increase in each grey scale, and the normalized axial velocity is evaluated by multiplying Δ by the number marked on the scale bar at the bottom of the figure. The cross-sectional average of the axial velocity corresponds nearly to 10 on the scale bar, since the measurements were conducted at the flow rate coefficient of about ϕ = 0.31 . The vertical dotted line is the reference position of a stall cell. The circumferential distance normalized by the blade spacing between the dotted line and the identification number on the right hand side of it is identical to T_p .

It can be seen in Fig. 11 that the axial velocity deficit regions appear over two blade spacings in the outer half of the annular flow passage, and they travel to the left at about 28 % of the rotor rotation in the relative frame to the rotor. This fact means the short length-scale stall cells of part-span type are rotating from left to right at 72 % speed in the stationary frame. In this paper, the terms of "front" (F) and "rear" (R) are used on the basis of the relative frame. Namely, the left hand side of the cell in the figure is the front side. The effect of the stall cell is considerably large even at a distance from the rotor by about 78 % of the axial chord length, and the minimum axial velocity becomes nearly zero in the cell. The axial velocity near the casing is slightly high at the front of the cell. This phenomenon is consistent with the velocity trace of a spike-type disturbance measured by Day (1993) and Silkowski (1995), in which abrupt decrease followed by slight increase in velocity occurs in a few blade spacing. On the top of Fig. 11, the velocity trace at r/r_t = 0.95 are shown for reference.

A large region of high axial velocity is located at the front and hub side of the stall cell. The shapes of the low and high velocity regions vary with the relative cell location T_p . Looking at the front of the right hand side cell in the figure, the slope of the contour lines between the low and high velocity regions is steeper at T_p = 0.2 than at T_p = 0.8 (compare Slopes 1 and 2). Another high velocity region is located near the circumferential position of 5 (refer to the number marked on the top horizontal line on the figure). This region does not travel in the relative frame because this is caused by a potential effect of the unstalled blade.

Figures 13 and 14 show the contour maps of the radial and relative tangential velocity components upstream of the rotor at T_p = 0.2. The figures are represented in the same manner to Fig. 11. The velocity components are normalized by the blade tip speed. The relative tangential velocity is taken as positive when it is in the opposite direction of the rotor rotation. In Fig. 13, the downward flow regions extend from the casing to hub in the same circumferential position of the axial velocity deficit regions. A region of slightly high upward flow exists at the front of the downward flow region. In Fig. 14, the regions of high tangential velocity are located at the front of the axial velocity deficit regions. The shapes of contour lines both for the radial and tangential velocity components change little with the relative cell location T_p (Figures are omitted.).

Three-dimensional feature of the flow field can be made clearer when the secondary flow velocity vector is defined by a component normal to the averaged exit flow angle in an unstalled flow region at each radial location. Figure 15 shows the secondary flow velocity vectors upstream of the rotor. They proceed to the left and downward direction near the stall cell, namely from the axial velocity deficit region to the high axial velocity region.

Flow field downstream of the rotor Figures 16 (a) to (d) show the contour maps of the normalized three velocity components and the secondary flow velocity vectors 8 mm downstream of the rotor trailing edge at T_p = 0.2. One can clearly distinguish the part-span stall cells from the unstalled blade wakes in these figures. Comparing the unstalled blade wakes between the 4th and 6th blade spacing (refer to the number marked on the top horizontal line on the figure), the wake is thicker as the stall cell approaches, because of increase in the angle

of attack. In the stall cell, the axial velocity deficit region with a strong reverse flow appears in the casing side and the increment in axial velocity occurs in the hub side to satisfy continuity. Looking at the right hand side cell, the low energy fluid discharges from the suction corner in the 3rd spacing, while from the pressure corner in the 2nd spacing. Both low energy fluids join with each other and make a big triangle reverse flow region as shown by a thick solid line (Fig. (a)). The radially outward flow occupies almost the 3rd spacing. For the 2nd spacing, however, the radial velocity component is not as high as that in the 3rd spacing (Fig. (b)). The relative tangential velocity is extremely low near the tip of the stall region, and a considerably high tangential velocity region appears along the pressure surface side (Fig. (c)). In Fig. (d), the secondary flow vectors proceed toward the reverse flow region. A counterclockwise and a clockwise circulating flow are observed in front and rear of the reverse flow region, respectively.

Comparing Fig. 16 (a) with Fig. 11, the axial velocity deficit regions upstream and downstream of the rotor are located almost at the same circumferential position. This phenomenon is similar to what was observed in the long length-scale stall cell by many researchers (Das and Jiang, 1984, Poensgen and Gallus ,1996, Palomba, et al., 1998).

With T_p increasing, the stall cell travels from right to left with changing in shape as if it penetrated the blade wakes. The contour maps of the three velocity components and the secondary flow velocity vectors at T_p = 0.8 are shown in Figs. 17 (a) to (d). It is found from Figs. (a) and (c) that the flow in the 2nd spacing is recovering and the stall in the 3rd spacing develops. The axial flow deficit region moves to 4th spacing, and is developing from the suction corner. The reverse flow region has two peaks: one is in the 3rd spacing and another is at the 4th blade suction corner. The radially outward flow region for the 4th spacing is larger than that for the 3rd spacing, although the axial velocity deficit region for the 4th spacing is considerably smaller (Fig. (b)). A clockwise circulating flow is observed again at the rear of the cell in the secondary flow map (Fig. (d)).

Casing wall pressure Figure 18 shows the variation of the ensemble averaged pressure distributions on the casing wall with T_p. The casing wall pressure p_w is represented by the pressure coefficient C_p defined as

$$C_p = (p_w - p_{oi})/(\rho u_t^2/2)$$

where p_w and ρ are the pressure and the air density of the inlet chamber, and u_t is the blade tip speed. The arrows U and D indicate the axial locations of the hot-wire surveys upstream and downstream of the rotor, respectively.

The most distinctive feature of the casing wall pressure is on the behavior of a bubble-like extremely low pressure region travelling ahead of the rotor from right to left. The bubble seems to have a leg which stands on the blade suction surface of the 3rd blade at T_p = 0.0, and on the 4th blade suction surface at T_p = 0.8 (refer to the number marked on the bottom horizontal line on the figure). Comparing the pressure distribution at T_p = 0.2 (or T_p = 0.8) with Fig. 11 and Fig. 16 (a) (or Fig. 12 and Fig. 17 (a)), the circumferential location of this bubble shifts by nearly one blade spacing in front of the axial velocity deficit regions. Namely, this bubble precedes the axial velocity deficit regions upstream and downstream of the rotor. On the right hand side of the bubble, a considerably high pressure region appears and the pressure hardly rises from inlet to exit of the (stalled) blade passage.

When looking at the blades in sequence of the number in parentheses marked in Fig. 18, one can see variation of the pressure distribu-

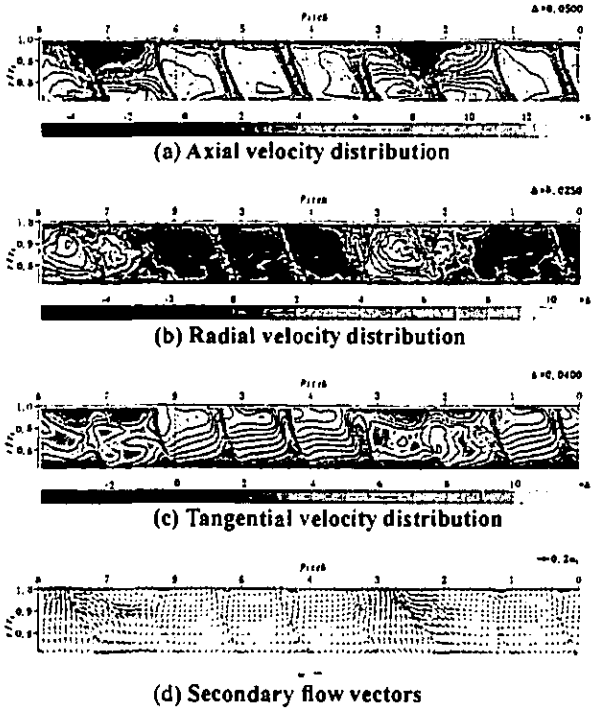

(a) Axial velocity distribution

(b) Radial velocity distribution

(c) Tangential velocity distribution

(d) Secondary flow vectors

Fig. 16 Flow field 8mm downstream of the rotor at T_p=0.2.

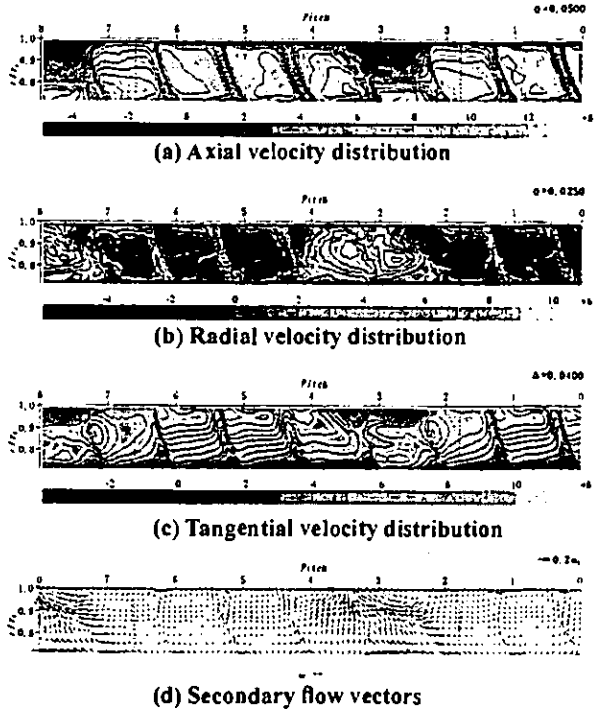

(a) Axial velocity distribution

(b) Radial velocity distribution

(c) Tangential velocity distribution

(d) Secondary flow vectors

Fig. 17 Flow field 8mm downstream of the rotor at T_p=0.8.

tion around a blade during a period of the stall cell traveling on a blade spacing. As the stall cell approaches from the right, a low pressure region grows gradually on the suction surface near the leading edge due to increase in the angle-of-attack (See the blades from (1) to (10) in order). Then, this low pressure region is linked to the low pressure bubble traveling ahead of the rotor, and merges in it to form a leg of the bubble (See from (11) to (15)). As the low pressure bubble travels toward the left hand side blade, the low pressure leg is stretched and moved toward the trailing edge with increasing the pressure level (See from (16) to (19)). Finally, it separates from the low pressure bubble and flows to the rotor exit (See from (20) to (23)). At T_p = 0.6 to 0.8, a comparatively low pressure region is discharged downstream of the rotor between the 2nd and 3rd blades, and a part of the low pressure region is discharged from the 3rd blade trailing edge. These two comparatively low pressure regions are corresponding to the two peaks of reverse flow region in Fig. 17 (a). Then they are linked together downstream of the 2nd blade at T_p = 0.0 and 0.2, which is corresponding to the triangle reverse flow region in Fig. 16 (a).

The pressure fluctuation has been evaluated by $\overline{p'^2}/(\rho u_t^2/2)^2$ where p' is the deviation from the ensemble averaged pressure at each measuring position. Figure 19 shows the distribution of pressure fluctuation on the casing wall at T_p = 0.2. It is extremely high in the low pressure bubble ahead of the rotor, and considerably high in the low pressure region inside the blade passage where the stall cell exists.

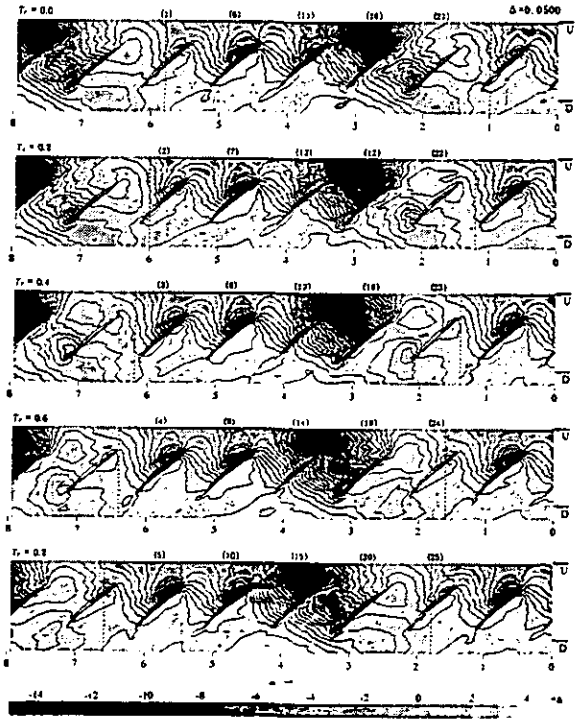

Fig. 18 Variation of ensemble averaged pressure distributions on the casing.

Fig. 19 Pressure fluctuation on the casing wall at T_p=0.2.

Flow model for short length-scale stall cell A flow mechanism of the short length-scale cell has been invesugated, by making animations for the velocity distributions upstream and downstream of the rotor and the pressure distribution on the casing wall, at intervals of T_p = 0.04. From observation of these animations the low pressure bubble traveling ahead of the rotor seems to be a key for the stall cell structure. According to the 2D numerical simulation of the long length-scale full-span stall by Saxer-Felici, et al. (1998), a strong vortex bubble forming ahead of the rotor makes such a low pressure region. Hoying, et al. (1998) also found a similar-shape of vortex ahead of the rotor when they captured a short length-scale stall of part-span type in their 3D numerical simulation, and they thought it was the tip clearance vortex moving upstream of the rotor leading edge. Referring to the results of these two simulations, the low pressure bubble shown in Fig. 18 must be a vortex.

In our experiment, however, behavior of the tip clearance vortex for the unstalled blades can not be captured clearly in the casing wall pressure distribution (Fig. 18), the axial velocity distribution (Figs. 16 and 17 (a)) and the secondary flow velocity vectors (Figs. 16 and 17 (d)) behind the rotor, because the tip clearance is considerably small (0.75 % of blade span, and 1 % of tip chord length).

A physically plausible explanation is that the low pressure bubble would be caused by a separation vortex moving upstream of the rotor. Accordiag to the vortex theory, bound vortices are distributed on an unstalled blade surface, which make a blade circulation (lift force). When leading edge separation occurs, a separation vortex is released from the blade surface to reduce the blade circulation. In the case of part-span stall, the separation vortex is only in the casing side. Its circulation may be on the order of blade circulation, if most of the blade circulation near the tip is lost due to stall. On the other hand, all the vortex-lines are attached to the blade surface in the hub side where separation has not occurred yet. According to continuity of the vortex lines, they must separate somewhere from the blade sucuon surface to be linked to the separation vortex near the casing. Namely, the vortex core consisting of these separated vortex lines spans from the blade suction surface to the casing wall. A spiral focus-type of separation will occur both on the suction surface and casing wall. The casing-side end of the vortex core moves ahead of the rotor to form the low pressure bubble with a strong circulation. It travels in the circumferential direction due to interaction with the blades.

(a) (b)

Fig. 20 Illustrations for the flow mechanism of short length-scale stall cell.

Behavior of this vortex is illustrated in Figs. 20 (a) and (b). The flow model presented in this illustration is consistent well with the experimental results mentioned in the previous sections.

In Fig. 18, the pressure is extremely lower at the low pressure bubble than in the blade passage, because the end of the separation vortex attaches itself to the casing wall, while another end is attached to the suction surface at a distant from the casing. As the separation vortex is considered to behave violently, likewise a tornado, the ensemble averaged low pressure region is considerably wide ahead of the rotor and in the blade passage. The extremely high level of pressure fluctuation in the low pressure bubble and the considerably high fluctuation level in the blade passage in Fig. 19 support this.

As the vortex bubble with a leg travels in the circumferential direction, the vortex leg is stretched and finally broken. This behavior corresponds to the variation of pressure distributions around the blades from (16) to (21) in Fig. 18. The broken vortex leg flows downstream and is discharged as low energy fluids downstream of the rotor, which corresponds to the pressure distributions around the blades from (22) to (25). On the suction surface of the blade located in the left hand side of the vortex bubble, a local separation will occur near the leading edge due to increase in the angle of attack, from where vortex lines are released in the flow. As the vortex bubble approaches to the blade, the released vortex lines are swallowed into the bubble. The separation grows to a large focus type separation, and the new vortex leg is generated. This behavior corresponds well to the variation of pressure distributions around the blades from (11) to (16) in Fig. 18.

The velocity distributions 8 mm downstream of the rotor in Figs. 16 and 17 can be explained by the present model. The reverse flow near the casing and the radial outward flow are induced by the vortex. At $T_p = 0.2$, the vortical flow just discharging from the 2nd blade suction surface causes a strong reverse flow at the suction corner and a strong outward flow in the 3rd blade spacing in Figs. 16 (a) and (b). The vortical flow, which is discharged from the passage between the 2nd and 3rd blades and is linked to the former vortical flow, has a slight effect on the radial flow velocity, partly because of location of the vortex center and partly because of decay. The slight effect can be seen in the clockwise secondary flow at the rear of the cell in Fig. 16 (d). At $T_p = 0.8$ (Fig. 17), the effect of the vortical flow is large on the axial velocity, but small on the radial velocity in the 3rd blade spacing, because the vortex center is located near the measuring plane. The reverse flow at the suction corner and the outward flow along the suction side of the 4th blade spacing are induced by the vortical flow at the trailing edge of the 3rd blade. The reverse flow region has two peaks, since the two vortical flows have not been linked to each other yet.

The velocity distributions 25.6 mm upstream of the rotor shown in Figs 11 to 15 can be also explained by the present model. The separation vortex is inclined as illustrated in Fig. 20. The induced velocity of the inclined vortex leg is related to the locations of the axial velocity deficit region and the high axial velocity region in Figs. 11 and 12. Namely, the separation vortex is located nearly parallel to the axial velocity contour lines in front of the axial velocity deficit region. The slope of the contour lines between the axial velocity deficit region and the high axial velocity region in Fig. 12 is more gradual than in Fig. 11, since the vortex is more stretched at $T_p = 0.8$ as conjectured from Fig. 18. The large axial velocity deficit is mainly due to the blockage effect of the low energy fluid with vortical structure in the blade passage. The effect of the induced velocity of the separation vortex appears also in the regions of high tangential velocity shown in Fig. 14, and can be seen more clearly in the secondary flow vectors shown in Fig. 15.

The flow mechanism of the short length-scale demonstrated above can be understand more clearly by observing the animations for the velocity distributions upstream and downstream of the rotor and the pressure distribution on the casing wall. The distinctive feature of the stall cell structure is on the low pressure bubble consisting of the separation vortex which travels ahead of the rotor. The elimination of this bubble should be a key for the active control of the spike-type rotating stall.

Conclusions

In the low-speed compressor test rig in Kyushu University, the multiple short length-scale stall cells appeared in a certain flow range. Then, formation and evolution of the multiple stall cells were investigated by the use of the cross-correlation function and the wavelet analysis for the casing wall pressure near the rotor leading edge. A short length-scale stall cell appeared at first, but did not grow rapidly in size. Alternatively, the number of cells increased to a certain stable state (a mild stall state) under a fixed throttle condition. In the mild stall state, the number of cells was five, the size was on the same order of the inception cell (a few blade spacings) and the rotating speed was nearly 72 % of rotor speed. With further throttling, the multiple short length-scale stall cells turned into a long length-scale wave overlapping the five short length-scale waves, then developed to a deep stall state with one big cell rotating nearly at 29 % of rotor speed.

The size, the wave form and the rotating speed of the stall cell were almost the same as what was appeared at the stall inception. They were also similar to those of the spike-type stall inception which had been reported in many literatures.

Then, time-dependent averages of the three-dimensional flow upstream and downstream of the rotor and the pressure distributions on the casing wall were obtained by the double phase-locked averaging technique, in which the outputs of a slanted hot-wire and high response pressure transducers were averaged phase-locked to both of the rotor and the cell rotation. The distinctive feature of the flow field was shown on the pressure distribution on the casing wall, namely an extremely low pressure bubble with a leg travelling ahead of the rotor. The leg was linked to a blade suction surface with changing the blade in turn as the pressure bubble traveled.

A model for the flow mechanism of the short length-scale stall cell has been presented based on the experimental results of the variation of the pressure distributions, which is summarized by:

(1) The separation vortex bubble with a leg standing on the blade surface travels ahead of the rotor in the circumferential direction.
(2) As it travels, the vortex leg stretches, breaks down, and finally discharges to the rotor exit, resulting in reverse flow regions near the casing downstream of the rotor.
(3) At the same time, a local separation occurs on the suction surface of the adjacent blade, from where the separated vortex lines are swallowed into the vortex bubble to generate a new vortex leg.

The above model reveals well the behavior of the three-dimensional velocity distributions measured upstream and downstream of the rotor. In concluding, the authors hope that further experiments or numerical simulations should be made to support the present model.

Acknowledgments

The authors are extremely grateful to Toshiba Co. for financial support of this experimental research work, and to Messrs. Maeda and Nakamura for helping the experimental work. They also appreciate the reviewers who recommended to combine two papers concerning the evolution of multiple stall cells and the structure of short length-scale cell.

References

Camp, T. R., and Day, I. J., 1998, "A Study of Spike and Modal Stall Phenomena in a Low-Speed Axial Compressors," ASME Journal of Turbomachinery, Vol. 120, pp. 393-401.

Day, I. J., 1993, "Stall Inception in Axial Flow Compressors," ASME Journal of Turbomachinery, Vol. 115, pp. 1-9.

Day, I. J., Breuer, T., Escuret, J., Cherrett, M. and Wilson, A., 1997, "Stall Inception and the Prospects for Active Control in Four High Speed Compressors," ASME Paper, 97-GT-281.

Das, D. K. and Jiang, H. K., 1984, "An Experimental Study of Rotating Stall in a Multistage Axial-Flow Compressor," ASME Journal of Engineering for Gas Turbines and Power, Vol. 106, No. 3, pp. 542-551.

Farge, M., 1992, "Wavelet Transforms and Their Applications to Turbulence," Annual Review of Fluid Mechanics, Vol. 24, pp. 395-457.

Garnier, V. H., Epstein, A. H. and Greitzer, E. M., 1991, "Rotating Waves as a Stall Inception Indication in Axial Compressors," ASME Journal of Turbomachinery, Vol. 113, pp. 290-301.

Hoying, D. A., Tan, C. S., Huu Duc Vo, and Greitzer, E. M., 1998, "Role of Blade Passage Flow Structures in Axial Compressor Rotating Stall Inception," ASME Paper, 98-GT-588.

Inoue, M., Kuroumaru, M., and Ando, Y., 1993, "Pressure Fluctuation on Casing Wall of Isolated Axial Compressor Rotors at Low Flow Rate," ASME Journal of Turbomachinery, Vol. 115, pp. 19-27.

Inoue, M., Kuroumaru, M., Furukawa, M., Kinoue, Y., Tanino, T., Maeda, S., and Okuno, K., 1997, "Controlled-Endwall-Flow Blading for Multistage Axial Compressor Rotor," ASME Paper, 97-GT-248.

Kuroumaru, M., Inoue, M., Higaki, T., Abd-Elkhalek, F. A., and Ikui, T., 1982, "Measurements of Three-Dimensional Flow Field Behind an Impeller by Means of Periodic Multi-Sampling of a Slanted Hot-Wire," Bulletin of the JSME, Vol. 25, No. 209, pp.1674-1681.

Mathioudakis, K. and Breugelmans, F. A. E., 1985, "Development of Small Rotating Stall in a Single Stage Axial Compressor," ASME Paper, 85-GT-227.

McDougall, N. M., Cumpsty, N. A., and Hynes, T. P., 1990, "Stall Inception in Axial Compressors," ASME Journal of Turbomachinery, Vol. 112, pp. 116-125.

Moore, F. K., and Greitzer, E. M., 1986, "A Theory of Post-Stall Transients in Axial Compression Systems: Part I, II," ASME Journal of Engineering for Gas Turbines and Power, Vol. 108, pp. 68-76, pp. 231-239.

Palomba, C., Puddu, P., and Nurzia, F., 1998, "3D Flow Field Measurement around a Rotating Stall Cell," ASME Paper, 98-GT-594.

Poensgen, C. A. and Gallus, H. E., 1996, "Rotating Stall in a Single-Stage Axial Flow Compressor," ASME Journal of Turbomachinery, Vol. 118, No. 2, pp. 189-196.

Saxer-Felice, H. M., Saxer, A., Inderbitzin, A., and Gyarmathy, G., 1998, "Prediction and Measurement of Rotating Stall Cells in an Axial Compressor," ASME Paper, 98-GT-67.

Silkowski, P. D., 1995, "Measurements of Rotor Stalling in a Matched and a Mismatched Multistage Compressor," GTL Report, No. 221, Gas Turbine Laboratory, Massachusetts Institute of Technology.

Weigl, H. J., Paduano, J. D., Frechette, L. G., Epstein, A. H., and Greitzer, E. M., 1997, "Active Stabilization of Rotating Stall and Surge in a Transonic Single Axial Compressor," ASME Paper, 97-GT-411.